

# Transient and steady-state behavior of space charges in multilayer organic light-emitting diodes

B. Ruhstaller<sup>a)</sup> and S. A. Carter

*Department of Physics, University of California, Santa Cruz, California 95064*

S. Barth, H. Riel, and W. Riess

*IBM Research, Zurich Research Laboratory, 8803 Rüschlikon, Switzerland*

J. C. Scott<sup>b)</sup>

*IBM Research, Almaden Research Center, San Jose, California 95120*

(Received 31 July 2000; accepted for publication 5 January 2001)

A numerical study of space charge effects in multilayer organic light-emitting diodes (OLEDs) is presented. The method of solving the coupled Poisson and continuity equations, previously established for single-layer polymer LEDs, has been extended to treat internal organic interfaces. In addition, we consider the transient current and electroluminescence response. We discuss the accumulation of charges at internal interfaces and their signature in the transient response as well as the electric field distribution. Comparison to experimental transient data of a typical bilayer LED based on tris(8-hydroxyquinolino)aluminum ( $\text{Alq}_3$ ) is provided and good agreement is found. Our results are consistent with commonly assumed operating principles of bilayer LEDs. In particular, the assumptions that the electric field is predominantly dropped across the  $\text{Alq}_3$  layer and that the electroluminescence delay time is determined by electrons passing through  $\text{Alq}_3$  to the internal interface are self-consistently supported by the results of the simulation. Moreover, the creation of emissive singlet excitons is found to be strongly confined to the  $\text{Alq}_3$  side of the internal interface and the emission zone width is dictated by the exciton diffusion length. Design principles for trilayer LEDs with improved power efficiency are also discussed. © 2001 American Institute of Physics. [DOI: 10.1063/1.1352027]

## I. INTRODUCTION

The discovery of bright organic electroluminescent diodes<sup>1,2</sup> has stimulated intense research in order to understand the physics of transport and recombination. While the general nature of the excited state and transport mechanisms in these novel semiconductors have been identified, further efforts to improve device performance are necessary and a quantitative numerical model is desirable to formulate design criteria. For the simplest device structure, an organic electroluminescent layer sandwiched between two metal electrodes, a number of theoretical studies regarding the injection and transport of charge carriers and their radiative recombination have been carried out;<sup>3–5</sup> however, an analytical solution to the bipolar transport and recombination problem is in general not available. In particular, the complex interplay between both field-dependent injection rates and charge carrier mobilities prevents a detailed theoretical prediction of device characteristics. Therefore, numerical solutions based on material parameters are a useful tool by which to understand and improve device characteristics.<sup>6–10</sup> Compared to polymer light-emitting diodes (LEDs) that achieve considerable efficiency even in single-layer structures,<sup>11</sup> efficient small molecule LEDs in general require a heterostructure

device design<sup>1</sup> that compensates for the imbalance of mobilities and injection rates and at the same time moves the recombination zone away from the electrodes in order to avoid luminescence quenching. Suitable multilayer designs<sup>9,10,12</sup> are critical for enhanced device performance and numerical methods are important to assist in this aim. Going beyond the study of steady-state current–voltage characteristics, transient electroluminescence studies provide additional insight into the device physics,<sup>13–17</sup> and are important for ac-driven display applications or suitable driving schemes for future electrically pumped lasing.<sup>18</sup>

In this article we discuss charge and recombination zone confinement effects in multilayer organic LEDs (OLEDs). We extended our model<sup>6,7</sup> to study multilayer structures and pulsed electroluminescence therein. We consider both transient<sup>13,15</sup> and steady-state space charge effects. Although comparison to experiment is only presented for small molecule based multilayer LEDs, the concepts developed are of a general nature and will apply equally to multilayered polymer LEDs. Some important differences between common polymer and small molecule based OLEDs result from different mobility ratios of electrons and holes. In the presence of a finite concentration of traps, the steady-state current is decreased but the charge carrier transit time remains, to a good approximation, unaltered. A detailed discussion of trap-controlled transient currents goes beyond the scope of this article and will be given elsewhere.<sup>19</sup>

<sup>a)</sup>Present address: IBM Research, Zurich Research Laboratory, 8803 Rüschlikon, Switzerland; electronic mail: bea@zurich.ibm.com

<sup>b)</sup>Author to whom correspondence should be addressed; electronic mail: jscott@almaden.ibm.com

The text is structured as follows. In Sec. II we describe the numerical model used and the specifics of treating multilayer structures. In Sec. III we discuss transient features in electroluminescence in general and for heterostructure devices. Section IV addresses steady-state effects by variation of applied bias and by modification of the cathode injection barrier, while Sec. V describes general principles of device design applied to trilayers. We conclude with a summary.

## II. THE MODEL

In this article we employ a numerical method previously established to describe current–voltage characteristics and spatial distributions of charge, electric field, and recombination rate in polymer LEDs.<sup>7</sup> The numerical solution of the continuity and Poisson equations has been extended to treat internal organic interfaces, and the dynamical response to a step change in voltage is obtained from the time-dependent iteration sequence.

### A. Transport and recombination

In the bulk, bipolar charge transport with field-dependent mobilities and Langevin bimolecular recombination is described by the following system of equations:<sup>6,8,20</sup>

$$J_e(x) = e\mu_e(x,E)n(x)E(x) + D(\mu) \frac{dn(x)}{dx}, \quad (1)$$

$$\frac{dE(x)}{dx} = \frac{e}{\epsilon\epsilon_0} [p(x) - n(x)], \quad (2)$$

$$\frac{dn(x)}{dt} = \frac{1}{e} \frac{dJ_e(x)}{dx} - r(x)p(x)n(x). \quad (3)$$

Here,  $n$  is the density of electrons,  $p$  the density of holes,  $E$  the electric field, and  $r$  the recombination rate coefficient. Equation (1) describes the net current  $J_e$  of electrons (holes analogous), composed of the drift and diffusion term, which are to satisfy the Poisson equation, Eq. (2). In Eq. (1)  $D$  is the Fickian diffusion constant related to the charge mobility by the Einstein relation  $eD = \mu kT$ .<sup>21</sup> The electron continuity equation, Eq. (3), contains the only term shared with its corresponding equation for holes, namely, the bimolecular recombination rate. We use the Langevin form  $r = (e/\epsilon\epsilon_0) \times (\mu_e + \mu_h)$  for the recombination rate.<sup>5,20</sup> Mobilities are taken to be field dependent with the Poole–Frenkel-like form

$$\mu(E) = \mu_0 \exp(\sqrt{E/E_0}), \quad (4)$$

where  $\mu_0$  is the zero field mobility and  $E_0$  the characteristic field.

### B. Injection and boundary conditions

In keeping with the continuum approach to the electrostatic behavior implied by Eqs. (1)–(4), we use a form for the currents at the electrodes and internal organic/organic interfaces that reflects the thermodynamic properties of the materials, such as the diffusion constant and mobility. This may be compared with the microscopic approach of Wolf *et al.*,<sup>22</sup> who considered details of the electronic structure at the molecular level and evaluated transition rates between

appropriate states. Within the framework of continuum electrostatics, current injection from metal contacts into organic semiconductor materials has been described previously<sup>23</sup> as a result of the interplay between thermionic injection and image charge recombination. In the presence of an applied electric field, Schottky barrier lowering occurs. Recent studies on injection into organic materials confirm the temperature and mobility dependence of the injection current and therefore are in favor of the thermionic injection model.<sup>24,25</sup> It has already been shown that contacts with injection barriers below 0.3 eV are able to maintain space-charge-limited currents (SCLCs) for typical operating voltage regimes at room temperature.<sup>7,8,26</sup> The same barrier height regime for ohmic behavior can be derived by considering the existence of SCL features in transient current; see Sec. III B. The actual values of the anode and cathode barriers are still a matter of considerable debate. Photoelectron spectroscopy reveals that the assumption of vacuum level alignment does not hold in general,<sup>27</sup> and that there is a theoretical suggestion of double layer formation.<sup>28</sup> As will be discussed in Sec. IV B, variation in injection barrier height influences the current balance and the internal charge distribution.

The electric field distribution is obtained through integration of the Poisson equation across the layers of total thickness  $L$  using the effective bias  $V_{\text{eff}} = (V - V_{\text{built in}}) = \int_0^L E(x) dx$  as constraint to determine the integration constant, i.e., the electric field due to space charges is superimposed on the applied field, which is corrected for the built-in field  $V_{\text{built in}}/L$ .

### C. Internal interfaces

In multilayered device structures, internal interfaces separate materials with differing molecular energy levels and charge mobilities. Each of these discontinuities can result in charge accumulation and cause redistribution of the electric field.<sup>9</sup> Molecular energy level discontinuities for electrons in the lowest unoccupied molecular orbital (LUMO) and holes in the highest occupied molecular orbital (HOMO) will be treated again in the context of transport in continuous media. We use an expression for the current across internal interfaces in analogy to the hopping process of transport, which has been thoroughly studied for organic semiconductors. As shown by Holstein and Emin<sup>29</sup> and previously by Marcus<sup>30</sup> and by Levich,<sup>31</sup> the hopping rate between two sites differing in energy by  $dE$  is proportional to

$$\exp\left(\frac{-(dE + E_p)^2}{4kTE_p}\right), \quad (5)$$

where  $E_p$  is the polaron binding energy,  $k$  the Boltzmann constant, and  $T$  the temperature. Rather than use this expression, which introduces an additional (and frequently unknown) parameter, we use the Miller–Abrahams<sup>32</sup> form in which the rate is activated for hops that increase the carrier energy (uphill) and is constant for downhill hops. This is strictly applicable only in the low-temperature weak coupling limit of Emin–Holstein theory. We also ran simulation sequences using an activated form for hops in both directions. The results differed insignificantly from those pre-

sented below, but the lack of a cutoff for downhill hops (analogous to the Marcus–Levich “inverted” region) led to numerical instabilities. Moreover, this form does not satisfy the condition of detailed balance. Hence for the current due to each carrier across an internal interface, we modify the drift and diffusion currents according to

$$J_{e,h}(J_{(e,h),\text{drift}} + J_{(e,h),\text{diff}}) = \begin{cases} \exp(-dE/kT), & dE > 0 \\ 1, & dE < 0 \end{cases}, \quad (6)$$

where the drift and diffusion currents are calculated using averaged properties of the materials to the left and right of the interface.

We do not introduce exciton diffusion across the internal interface since excitonic energy transfer in triphenylamine derivative (TPD)/tris(8-hydroxyquinolino)aluminum (Alq<sub>3</sub>) bilayers is unlikely<sup>33</sup> unless TPD is doped with dye molecules.<sup>34</sup> Similarly, no exciplex-like recombination across the interface is implemented. For a discussion of energy level alignment at organic/organic interfaces, see, for instance, Ref. 27.

#### D. Singlet excitons: Generation, diffusion and decay

In addition to the Langevin recombination rate, we calculate the density of singlet excitons  $S$  by considering their generation, diffusion, and decay which allows the temporal and spatial evolution of luminescence to be studied. In contrast to the radiative decay time, the exciton diffusion constant is not easily accessible experimentally but can be estimated, for instance, by modeling the thickness dependence of the efficiencies of photovoltaic devices.<sup>35,36</sup> The continuity equation for excitons, including generation, diffusion, and decay, is

$$\frac{dS(x,t)}{dt} = \gamma r(x,t)n(x,t)p(x,t) + D_S \frac{d^2S(x,t)}{dx^2} - \frac{S(x,t)}{\tau}, \quad (7)$$

where  $\gamma = 1/4$ , following the (simple) spin statistics argument and assuming Fickian diffusion.<sup>37</sup> We use the diffusion constant  $D_S = l^2/\tau$ , with  $l$  being the diffusion length and  $\tau$  the exciton lifetime. Given that the first term on the right-hand side is replaced by a dirac-delta-like steady-state source term upon turnon at  $t = t_0$ ,  $\xi \delta(x - x_0) \theta(t - t_0)$ , Eq. (7) can be solved analytically. The exciton distribution in equilibrium decays exponentially according to

$$S(x, t \rightarrow \infty) = \frac{\xi \tau}{l} \exp\left(-\frac{x - x_0}{l}\right), \quad x > x_0. \quad (8)$$

We note that the exponential decay is determined by  $l$  only, whereas the exciton density at  $x_0$  is dictated by the decay time  $\tau$ . Therefore, in this special case,  $l$  can be considered as the emission zone width.

Exciton quenching near electrodes was found to occur for poly(phenylenevinylene) (PPV)-type polymers<sup>38</sup> and Alq<sub>3</sub> alike.<sup>39</sup> The presence of metal electrodes is believed to increase the radiative lifetime significantly and therefore lower the luminous efficiency by allowing nonradiative decay channels to play a dominant role.<sup>38</sup> For PPV-type poly-

mers the quenching zone extends as far as 20 nm from the electrode.<sup>38</sup> Unless the recombination zone approaches either the anode or cathode, exciton quenching plays a minor role in multilayer LEDs, and we therefore do not discuss this additional concern.

#### E. Numerical solution

Equations (1)–(4), (6), and (7) are solved numerically by discretizing space and time. The device structure is divided into cells with widths comparable to the hopping site separation ( $\sim N_c^{-1/3} = 0.4$  nm,  $N_c$  being the density of chargeable sites). To account for the major discontinuities in mobility parameters at internal interfaces,<sup>40</sup> a nonuniform cell-width approach<sup>41</sup> is implemented with smaller widths near interfaces in order to improve accuracy with reduced computation time. Because charge densities are defined in the center of cells while the electric field, mobilities, and currents are defined at cell boundaries, the extension from single to multiple layers requires only appropriate treatment of the organic interfaces as described in Sec. II C.

The coupled set of equations is solved iteratively starting with an empty device and assuring that the time step is one order of magnitude smaller than the fastest transit time across a cell in the device at any given iteration step. For the simulation of current–voltage curves, the distribution of previous bias is used as the initial condition for the subsequent voltage setting. The system is considered to be in equilibrium and the iteration terminated when the average local deviation is a small fraction, typically  $10^{-5}$ , of the total current.

#### F. Parameters

The parameters required as input to the simulation are the mobility and energy level parameters for each layer and the work functions of the metal contacts. The determination of field-dependent mobilities is crucial for a successful quantitative description of transient and steady-state operation of OLEDs. Common techniques are time-of-flight (TOF) measurements<sup>42</sup> and analysis of current–voltage characteristics<sup>43</sup> in single-layer devices. If space-charge effects prevail (i.e., the contacts are ohmic), mobilities may also be determined by mapping the transient current peak position to the transit time of the predominant carrier,<sup>44</sup> according to Eq. (9), as discussed below.

Similarly, the electroluminescence (EL) delay time can be used to estimate the mobility of the faster carrier<sup>14,45</sup> in the luminescent layer. In a  $N, N'$ -di(naphthalene-1-yl) =  $N, N'$ -diphenyl-benzidine (NPB)/Alq<sub>3</sub> bilayer LED, the assumption that the delay time is determined by electrons passing through the entire layer of Alq<sub>3</sub>, driven by the applied bias dropping entirely across Alq<sub>3</sub>, is manifested by spectral evidence that recombination initially occurs near the internal interface.<sup>46</sup> This assumption is self-consistently supported by the results of the simulation that will be discussed in Secs. III and IV. We used the field-dependent electron mobility of Alq<sub>3</sub> determined in this way by Barth *et al.*,<sup>14</sup> see Table I. The hole mobility in Alq<sub>3</sub> is assumed to be 10 times smaller than the electron mobility, using the same field de-

TABLE I. Mobility and energy level parameters for TPD and Alq<sub>3</sub> as used for the simulation.

Layer material	$\mu_{0,e}$ (cm <sup>2</sup> /V s)	$E_{0,e}$ (kV/cm)	$\mu_{0,h}$ (cm <sup>2</sup> /V s)	$E_{0,h}$ (kV/cm)	HOMO (eV)	LUMO (eV)
TPD	$10^{-8}$	100 000	$3.2 \times 10^{-3}$	14 800	5.4	2.5
Alq <sub>3</sub>	$1.2 \times 10^{-6}$	1959	$1.2 \times 10^{-7}$	1959	5.7	3.0

pendence, which is compatible with the recombination zone occurring near the internal interface.<sup>1,46,47</sup> For comparison, various field-dependent electron and hole mobility parameters of Alq<sub>3</sub> have been reported in the literature. Kepler *et al.*<sup>48</sup> used a TOF technique and found the hole mobility to be nearly two orders of magnitudes smaller than the electron mobility. Using the same technique, Naka *et al.*<sup>49</sup> found an electron to hole mobility ratio exceeding 100. Mückel *et al.*<sup>45</sup> analyzed the EL delay time in a sandwich structure to find a hole mobility that increases more strongly with field than the electron mobility does and at typical operating fields therefore approaches that for electrons. For the hole-transport layer, hole mobility parameters determined for *N,N'*-diphenyl-*N,N'*-(3-methylphenyl)-1,1'-biphenyl-4,4'-diamine (TPD) by TOF measurements were taken from the literature<sup>50</sup> and electron mobility was chosen to be small compared to that in Alq<sub>3</sub>.

In contrast to Alq<sub>3</sub>-based LEDs, polymer LEDs based on PPV derivatives typically have comparable mobilities for electrons and holes as well as HOMO and LUMO levels matchable to electrode work functions. Contacts are therefore more nearly ohmic and charge injection is closer to balance. Also, the bipolar transient current does not show any overshoot and recombination is, in general, not limited to electrode interfaces.

For excitons we use a lifetime of 16 ns, which is the radiative lifetime typically found for Alq<sub>3</sub>,<sup>47</sup> and a diffusion length of 10 nm.<sup>51</sup> The material parameters used in Secs. III and IV are listed in Table I. Those used in the discussion of trilayer designs in Sec. V are summarized in Table II.

### III. TRANSIENT ELECTROLUMINESCENCE

Here and in Sec. IV we present simulation results for bilayer structures composed of a 50-nm-thick electron-transport layer (ETL), in which recombination also occurs, and a 65-nm-thick hole-transport layer (HTL) and compare them with experiment. Experimentally, a third thin layer of copper phthalocyanine (CuPc) is often deposited on top of the transparent anode and below the HTL for improved device stability. In the simulation this layer was omitted in this first study for the sake of simplicity, which we justify by the simulated performance being relatively insensitive to slight variations of the anode injection barrier height. The anode is sufficiently ohmic, and hole mobility in the HTL is high.

#### A. Experiment

The organic layers are evaporated on top of a glass substrate patterned with a transparent anode [indium-tin-oxide (ITO)]. The cathode is commonly formed by coevaporation of magnesium and silver (90% Mg:Ag). Transient EL mea-

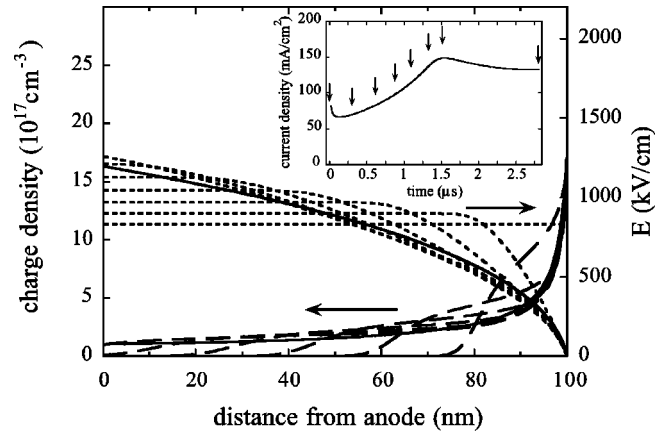


FIG. 1. Transient distributions of the electric field and charge densities upon application of 10 V to a single layer (100 nm) of Alq<sub>3</sub> with an electron injection barrier of 0.3 eV. The continuous lines show the distributions close to steady state at 2.8  $\mu$ s. Corresponding instants in time are indicated in the inset by arrows in the current transient.

surements are performed using a pulse source, a Hamamatsu photomultiplier, and Tektronix digital oscilloscopes. The *RC* time of this setup including the OLED investigated is 0.2  $\mu$ s. The device fabrication and the experimental procedures were described previously in more detail in Ref. 14.

#### B. Transient space-charge-limited current

We simulate transient monopolar currents as a test of the accuracy of the algorithm prior to studying EL transients and show that our numerical method reproduces analytical results for the time-dependent monopolar current in single-layer devices. Transient behavior of SCLCs in organic semiconductors was described theoretically, ignoring diffusion, by Many and Rakavy<sup>52</sup> and by Helfrich and Mark.<sup>53</sup> In a monopolar and single-layer configuration, the carrier transit time is shorter than in the absence of space-charge effects due to the enhancement of the electric field at the leading edge of the carrier packet. This transit time reduction is given by

$$t_{tr} = 0.786L/\mu E, \quad (9)$$

where  $L$  is the layer thickness,  $\mu$  the carrier mobility (here, field independent), and  $E$  the applied electric field. The transient current overshoots its steady-state value by a factor of 1.21 and starts at 0.44 times the steady-state value.<sup>52,53</sup> Upon reaching steady state, the electric field and the charge density assume the familiar Mott-Gurney solution, i.e., proportional to  $x^{1/2}$  and  $x^{-1/2}$ , respectively, where  $x$  is the distance from the injecting electrode. Transient SCLCs (TSCLCs) can be used to determine the charge carrier mobility<sup>44</sup> and to study the quality of the injecting contact.<sup>54,55</sup> The temporal evolution of the internal electric field and the carrier densities is illustrated for an electron-dominated single-layer Alq<sub>3</sub> device in Fig. 1 upon turnon of a 10 V step voltage. Electrons travel from the cathode on the right-hand side of Fig. 1. Before equilibrium is achieved (continuous lines in Fig. 1), the leading charges experience an electric field that is always greater than the average field, in this case 830 kV/cm including the built-in contribution, and reaches a maximum at the time of arrival at the other electrode. This mechanism is responsible

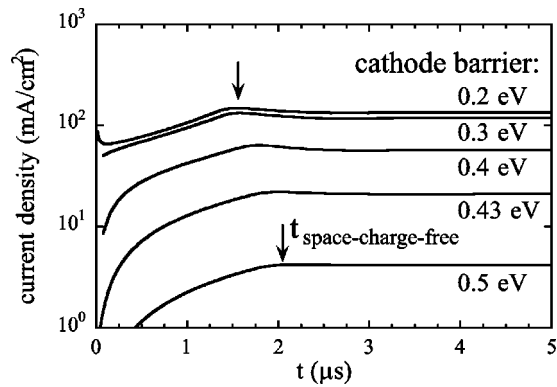


FIG. 2. Transient current of a 100-nm-thick single-layer Alq<sub>3</sub> LED for various electron injection barriers (0.2, 0.3, 0.4, 0.43, and 0.5 eV). The current peak position shifts to longer times as the barrier is increased and eventually reaches the space-charge-free (injection-limited) transit time  $t = 2.03 \mu\text{s}$ , indicated by the arrow, as can be calculated using the average electric field.

for the transit time reduction.<sup>56</sup> An ohmic contact is required for the observation of a TSCLC peak as is illustrated in Fig. 2 by a variation of injection barrier height. Injection-limited transients are characterized by a much lower initial current, the absence of a transient current peak, and a longer (space-charge-free) transit time that approaches  $L/\mu E$ . Similar arguments apply to bilayer LEDs; see Sec. IV B. The beneficial use of lithium fluoride (LiF) in forming an ohmic contact was demonstrated previously<sup>57–60</sup> and confirmed by TSCLC measurements of single-layer Alq<sub>3</sub> diodes.<sup>55</sup> The above results are slightly modified in the case of field-dependent mobilities.<sup>61</sup> Further, diffusion is responsible for rounding of the cusp in the Many–Rakavy solution<sup>52</sup> because of broadening of the carrier front and therefore the distribution of arrival times.<sup>19,61</sup>

### C. Pulsed electroluminescence

Pulsed EL has been studied theoretically<sup>17</sup> and quite extensively experimentally, e.g., in Refs. 13, 14, 16, and references therein. Here we present numerical simulations of bilayer devices and find mechanisms that we compare to those established for single-layer devices.<sup>13</sup>

In Fig. 3(a) the experimental current and EL response of an ITO/CuPc (20 nm)/NPB (45 nm)/Alq<sub>3</sub> (50 nm)/Mg:Ag LED to 5  $\mu\text{s}$  pulses at a repetition frequency of 1 kHz and at pulse heights of 6 (dashed line), 7 (short-dashed line), and 8 V (continuous line). Using this device structure, electron mobility parameters were extracted from TSCLC and TOF measurements.<sup>14</sup>

For comparison, we simulated a TPD/Alq<sub>3</sub> bilayer structure with a 0.5 eV electron and 0.4 eV hole injection barrier, respectively. The mobility parameters used are given in Table I. The simulated device has the same Alq<sub>3</sub> layer (50 nm) and total (115 nm) thickness as the experimental device [Fig. 3(a)]. We calculate the response to one pulse period of a rectangular voltage step and subsequent resetting to zero. In Fig. 3(b) the calculated transient current and EL response to a voltage steps of 6, 7, and 8 V are shown. The initial high current and fast decay are due to the fast holes crossing the TPD layer to the internal interface. The negative current upon turnoff is bigger in magnitude for the higher initial voltage, since more charges have accumulated in the device.

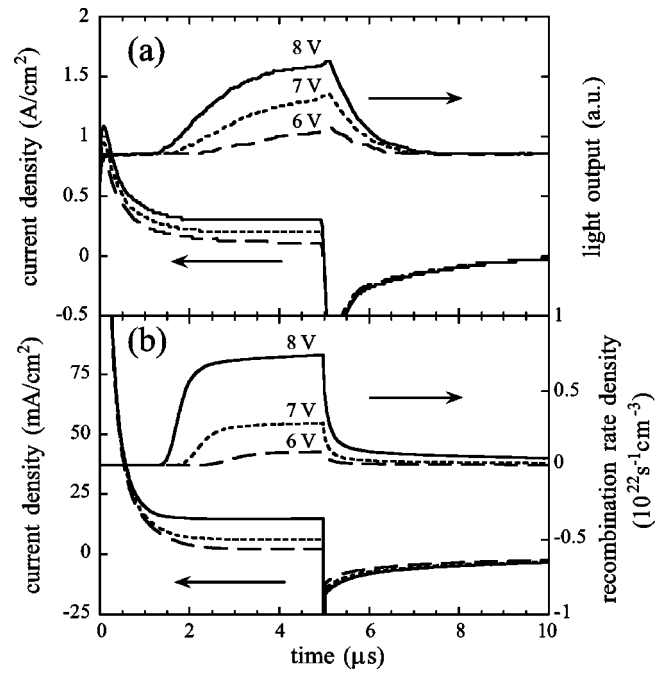


FIG. 3. (a) Experimental current and electroluminescence responses of an ITO/CuPc (20 nm)/NPB (45 nm)/Alq<sub>3</sub> (50 nm)/Mg:Ag LED to 5  $\mu\text{s}$  pulses at a repetition frequency of 1 kHz and at pulse heights of 6 (dashed line), 7 (short-dashed line), and 8 V (continuous line). (b) Simulated transient electroluminescence response of a bilayer TPD (65 nm)/Alq<sub>3</sub> (50 nm) LED to voltage pulses of 6 (dashed line), 7 (short-dashed line), and 8 V (continuous line). For reference, the calculated current transient is also shown. Characteristic features that are reproduced: fast and slow rises, delayed electroluminescence and negative current upon turnoff due to charge removal driven by space charge, and built-in field [compare to (a)].

The delay time for EL is entirely determined by the arrival of electrons at the internal interface and varies with applied bias, as expected. While the fast initial rise can be attributed to the establishment of a high recombination rate density at the Alq<sub>3</sub> side of the internal interface, the slow later rise is due to increasing penetration of holes into the Alq<sub>3</sub> layer. Given that the turnon delay time is reproduced correctly [compare to Fig. 3(a)], we conclude that the electric field is predominantly dropped across the ETL (Alq<sub>3</sub>). The ratio of electric field strength in the ETL compared to that in the HTL will be discussed in Sec. IV A. We note some discrepancy between experiment and simulation in the steepness of the fast rise, possibly arising from too many electrons piling up at the internal interface due to overestimation of the internal electron barrier height. Treusch *et al.*<sup>62</sup> determined a LUMO offset at an TPD/Alq<sub>3</sub> interface of only 0.1 eV by x-ray photoabsorption. By contrast, the hole pileup determines the transit time of electrons across Alq<sub>3</sub> through the enhanced electric field in that layer. Better agreement with experiment for the current magnitude can be achieved by adjusting the injection barrier heights, which does not alter the EL delay time. Thus, to match the simulated current to the experimental one, a cathode barrier of only 0.43 eV needs to be chosen even though the nominal barrier is as high as 0.6 eV. Significant deviations from nominal barrier heights due to interfacial dipole layers at the injection contacts have been found previously.<sup>27</sup> The simulated transient currents of the single-layer Alq<sub>3</sub> device in Fig. 2(a) illustrate

the steady-state current variation with assumed injection barrier height. EL decay upon turnoff will be discussed in Sec. E.

#### D. Temporal recombination zone shift

Next, we shall consider the charge and recombination density as well as the electric field profile as they evolve towards equilibrium after turnon. In multilayer OLEDs charge carrier mobilities can vary by several orders of magnitude from layer to layer. Therefore, the faster charges will penetrate the device and modify the electric field distribution well before the other charge has built up a significant density within the bulk. As a result, the transient current peaks on a very early time scale and is followed by a steep decay prior to equilibrating [compare to Fig. 2(b)]. In the case of common bilayer OLEDs based on Alq<sub>3</sub>, this effect is believed to facilitate the injection of electrons, because holes reach the internal interface well in advance and cause the electric field to be greatest in the Alq<sub>3</sub> layer. The experimental determination of the internal electric field is a nontrivial issue.<sup>15,27,62–66</sup>

As was pointed out by Pinner *et al.* for a single-layer structure,<sup>15</sup> the position and magnitude of the maximum electric field may vary during equilibrium. The penetration of the slower carrier smooths the electric field distribution. In the transient EL of the bilayer device, further equilibration is reflected by a slow approach to equilibrium dictated by the low mobility of holes in Alq<sub>3</sub>. The interpenetration of hole and electron populations results from the low cross section inherent in Langevin recombination. Equilibration is completed when holes either reach the cathode (a cathode-limited device, leading to low current balance) or encounter a high density electron space-charge region near the cathode, which results in a high probability of recombination. In our bilayer device we find an additional feature. While the initial EL may occur at a position in the emissive layer that is determined by the mobility ratio of electrons to holes therein, the charge accumulation at the internal interface eventually becomes dominant and the recombination shifts to the Alq<sub>3</sub> side of the internal interface. In Fig. 4 the electric field and recombination rate density are shown. At turnon (0.75  $\mu$ s), the recombination rate peaks in the Alq<sub>3</sub> bulk, 5 nm from the interface. The continuing pileup of electrons at the internal interface causes a shift of this peak position toward the interface and the fast rise in EL (inset of Fig. 4). Correspondingly, although the electric field at turnon is highest 5 nm from the interface, the electron pileup results in a local peak in the electric field at the interface, but further penetration of holes into Alq<sub>3</sub> causes the electric field peak position to shift into the bulk.

We note that in the case of Fig. 4 the recombination rate density is confined to a very narrow region and the approximation by a Dirac-delta source is acceptable. Figure 5 shows the corresponding singlet exciton distribution at various times after turnon (compare to Fig. 4). The exciton distribution approaches a steady state near 2  $\mu$ s. The inset shows the exciton density on a logarithmic scale and reveals the exponential decay with a constant of 10 nm, in agreement with the assumed exciton diffusion length and the analytical solu-

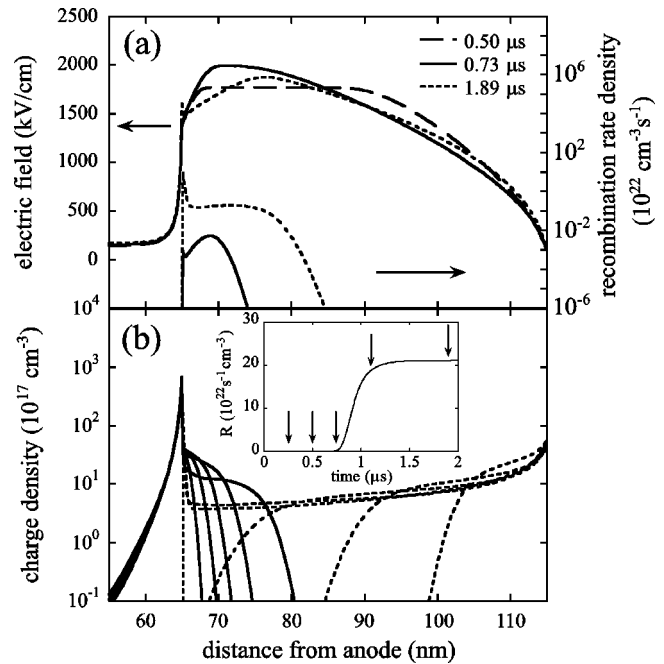


FIG. 4. (a) Evolution of electric field and recombination zone for a bilayer TPD (65 nm)/Alq<sub>3</sub> (50 nm) device upon application of a 10 V pulse using a cathode injection barrier of 0.2 eV (same as in Fig. 11). (b) The charges first meet at around 70 nm, 5 nm from the internal interface in the Alq<sub>3</sub> layer, giving rise to a broad recombination rate density peak. During the fast rise in electroluminescence [see inset in (b)], the recombination peak position shifts towards the internal interface. Along with this, electrons pile up at the internal interface and a local peak in the electric field at the interface emerges because of the high hole density on the opposing side of the interface.

tion, Eq. (8). In this case, the doping method used to determine the emission zone width actually measures (and may modify) the exciton diffusion length. In the literature, several studies on the recombination and emission zone in Alq<sub>3</sub>-based bilayer LEDs have been reported.<sup>47,67–69</sup> The initial study by Tang *et al.*<sup>47</sup> reported 5 nm for the recombina-

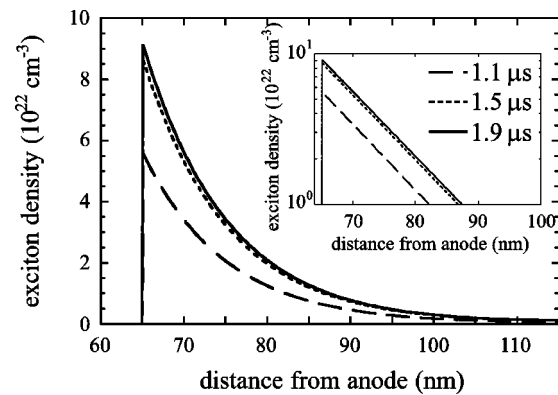


FIG. 5. Singlet exciton density profiles obtained as the solution to Eq. (7) at different times for a bilayer TPD/Alq<sub>3</sub> device after application of a 10 V pulse (same parameters as in Fig. 4). Due to strong confinement of the recombination rate density close to the internal interface (see Fig. 4), the exciton density and therefore emission profiles decay exponentially with distance from the interface, similar to the prediction for a Dirac-delta-like source at the interface. The inset shows the density on a logarithmic scale and reveals the exponential decay with a constant of 10 nm, in agreement with the assumed exciton diffusion length.

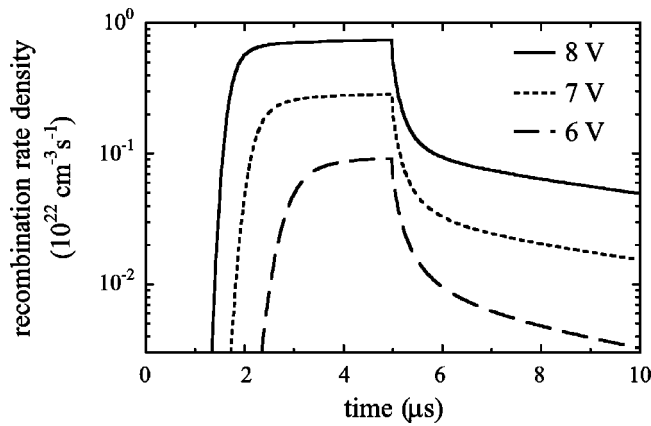


FIG. 6. Simulated transient recombination rate densities [same as in Fig. 3(b)] for 6, 7, and 8 V plotted on a logarithmic scale. While the electroluminescence drops to different values for different initial biases, the time constant of the slow decay alters only marginally, and is related to the detailed residual space-charge distribution.

tion zone width and about 20 nm for the emission zone width. Lam *et al.*<sup>67</sup> estimated the emission zone to extend at least 20 nm into the bulk of Alq<sub>3</sub> by a delta-doping method. Yamashita *et al.*<sup>68</sup> used a doping region of varying thickness to conclude that the recombination zone width was 10 nm, and Matsumura and Jinde<sup>69</sup> derived an emission zone width of 20 nm, which shrinks as the devices degrade. Indirect experimental evidence for the equilibration process of exciton distribution, as shown in Fig. 5, was found in rubrene-doped Alq<sub>3</sub> multilayers by a temporal analysis of the relative spectral contributions of rubrene and Alq<sub>3</sub>.<sup>46</sup>

### E. Delayed electroluminescence upon turnoff

While the turnon dynamics are dictated by the buildup of space charge in the device, delayed EL upon turnoff is probing the slow removal thereof. The intensity of delayed EL is determined by the amount of residual space charge in the device. Figure 6 shows the simulated EL transients of Fig. 3 on a logarithmic scale for 6, 7, and 8 V. An initial drop upon turnoff is followed by a fast and slow EL decay. The long decay constant changes only slightly for different biases and is related to details of the space-charge field distribution.

Upon turnoff, the electric field in the device is a superposition of the built-in field and the space-charge field only. Charge storage effects can either be studied by applying a prebias in the time between pulses,<sup>14</sup> or by altering the duty cycle and thereby probing the residual charge upon turnoff.<sup>16</sup> Additionally, the internal electric field at the position of maximum recombination can be probed by analyzing the drop in EL upon turnoff.<sup>15</sup>

It is commonly assumed that the total field upon turnoff points in the opposite direction to the previously applied field. However, if the accumulated space charge results in a field that exceeds the built-in potential in magnitude, then the total field may change sign locally. This is more likely to occur in multilayer devices since the space-charge field exhibits strong nonuniformity due to charge accumulation at internal interfaces. As a result, in regions with positive electric field, charges continue to interpenetrate each other and

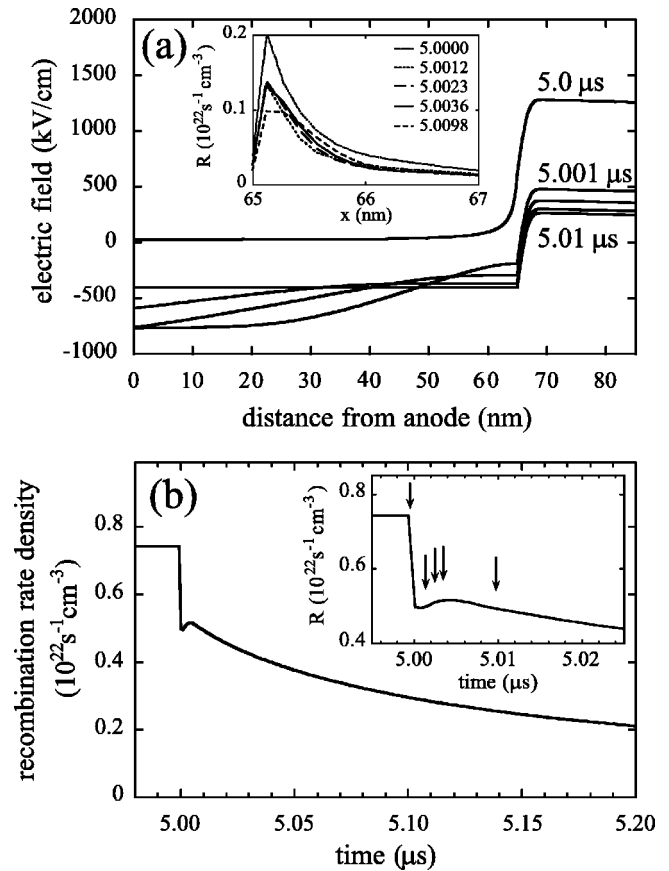


FIG. 7. Early time scale upon turnoff after application of a 10 V pulse for 5  $\mu$ s to a TPD/Alq<sub>3</sub> bilayer device with a 0.5 eV cathode barrier height. (a) Spatial dependence of electric field and recombination and (b) temporal dependence of recombination. During the fast removal of holes through the HTL, the recombination rate density increases temporarily, due to charge interpenetration on the Alq<sub>3</sub> side of the interface [see inset to (a)], and results in a transient rise in recombination [expanded in the inset to (b)].

recombine, while in regions with negative electric field, charges move back toward the electrodes they were injected from. To illustrate this mechanism, let us consider the turn-off regime of the 8 V transient of Figs. 3 and 6, respectively. Figure 7 depicts the early time regime after application of a 5  $\mu$ s pulse. As the applied field is switched off, the field changes sign in the HTL but remains positive in most of the ETL. Just to the right of the internal interface, where the highest electron charge density has accumulated, the electric field goes negative, pulling holes back to the HTL and electrons towards the bulk of Alq<sub>3</sub>. This interpenetration gives rise to a local and temporal recombination rate increase as the inset of Fig. 7(a) shows and is accompanied by the removal of the hole accumulation layer at the HTL side of the internal interface. The fast removal of holes is manifested in the electric field profiles; see Fig. 7(a). The short-lived rise in recombination is evident in the recombination rate density transient; see Fig. 7(b). The time scale of this effect is correlated to the quick removal of holes from the internal interface through the HTL. The interpretation is consistent with the observation that the time delay of the transient peak in the recombination rate density is only marginally dependent on the hole mobility in Alq<sub>3</sub> as has been checked with 0.1 and 0.01 mobility ratios in Alq<sub>3</sub>. Our simulation shows a

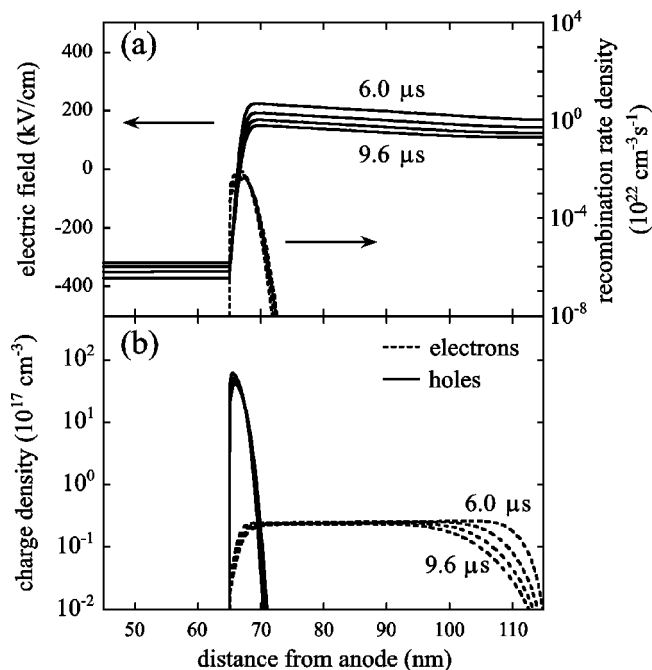


FIG. 8. Long time scale upon turnoff of the same device as in Fig. 7 (distributions at 6, 7.2, 8.4, and 9.6  $\mu\text{s}$  shown). As a result of the strongly nonuniform space-charge field that remains upon turnoff, (a) the electric field remains positive in most of the  $\text{AlQ}_3$  layer. Therefore (b) the residual charges in the  $\text{AlQ}_3$  layer continue to recombine. The charges and the recombination zone are no longer confined to the internal interface during the long-lived decay.

transient peak in the recombination rate that does not overshoot its steady-state value. Turn-off spikes in EL have been reported in polymer<sup>70</sup> and small molecule<sup>71</sup> based bilayer LEDs. In the former case the overshoot occurred on a ms time scale, compared to a sub ms time scale in the latter. Both interpretations relied on interfacial phenomena (interpenetration of materials in the former, discharging of the interfacial layer in the latter case), but further insight into the details of the dynamics is desirable.

On a longer time scale, the charge density diminishes by recombination in a relatively broad region near the internal interface. This is shown in Figs. 8(a) and 8(b), respectively, for the electric field and recombination rate density as well as for the electron and hole density. The time constant of this long-lived EL is determined by the higher residual charge mobility, in this case the electron mobility, as is confirmed by a variation of the mobility ratio from 0.1 to 0.01. A study of charge storage effects by means of duty cycle variation is underway.

#### IV. STEADY-STATE SPACE-CHARGE EFFECTS

##### A. Charge accumulation and electric field enhancement

We will now discuss the bias dependence of space-charge effects in bilayer structures, described in Sec. III C. The difference between the high hole mobility in the HTL and the low electron mobility in the ETL increases the electric field in the ETL significantly above the average field. The accumulation of charges on either side of the internal

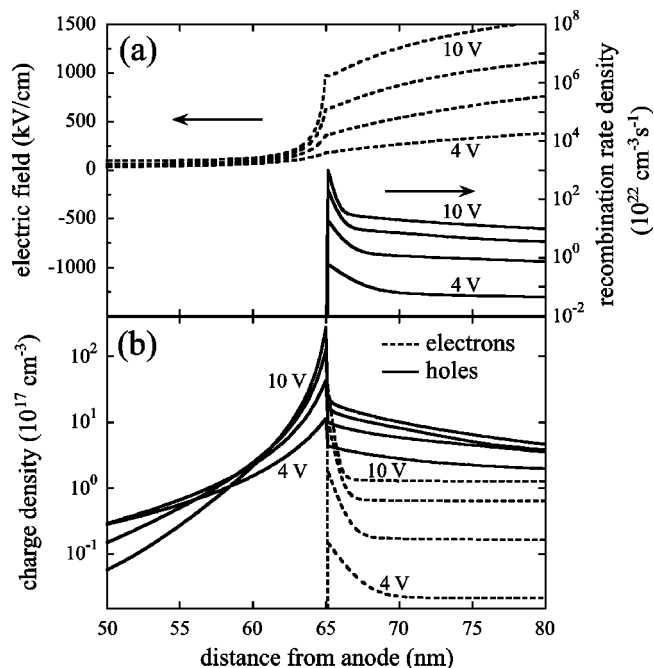


FIG. 9. (a) Electric field and recombination rate density as well as (b) charge density distribution in a bilayer TPD (65 nm)/ $\text{AlQ}_3$  (50 nm) device with a 0.5 eV cathode barrier at various biases (4, 6, 8, and 10 V). As the voltage is increased, the confinement of holes to the internal interface is enhanced, causing the electric field ratio from  $\text{AlQ}_3$  vs TPD to increase. Similarly, the electron pileup on the  $\text{AlQ}_3$  side narrows with increasing bias, resulting in enhanced confinement of the recombination rate density; see (a).

interface causes a local peak in the electric field distribution. In Fig. 9 the electric field distribution is shown together with the recombination zone for biases from 4 to 10 V. Using an electron injection barrier of 0.5 eV, the accumulation of holes increases with increasing bias, which results in a bigger difference between the electric fields in the HTL and the ETL. Experimentally, direct probing of the internal potential distribution with a sandwiched third electrode was reported by Hiramoto *et al.*,<sup>63</sup> whereas indirect electroabsorption techniques allow the determination of the average electric field in individual layers.<sup>64,65</sup> In support of our findings, in these studies, using equivalent  $\text{AlQ}_3$ -based bilayer LEDs, we have found the electric field across the  $\text{AlQ}_3$  layer to be enhanced by a factor of approximately 5–10 with respect to the field across the HTL.

The recombination rate density profile remains confined to the internal interface for the bias range considered and narrows for increasing bias correlated with a narrowing electron pileup. Similarly, the hole accumulation is enhanced at higher bias.

##### B. Efficiency versus bias

The device quantum efficiency is proportional to the current balance factor  $b$  and to other factors that are not related to the electrical properties of the device.<sup>5</sup> Numerically, the current balance factor  $b$  in equilibrium can be evaluated using the electron, the hole, or the recombination current:

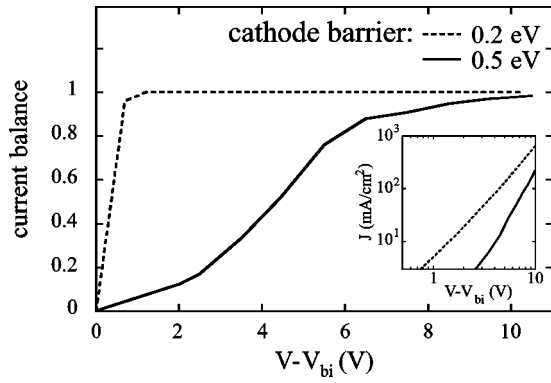


FIG. 10. Current balance vs voltage curve for bilayer TPD/Alq<sub>3</sub> devices with different electron injection barriers, after correction of the built-in potential (1.8 and 1.5 eV, respectively). The device with the small injection barrier (0.2 eV) exhibits ideal current balance independent of the applied voltage, whereas the device with the high injection barrier (0.5 eV) achieves ideal current balance only at high bias. The inset shows a log–log plot of the corresponding current–voltage curves. The apparent power is higher (exceeding a power of 3) for the contact-limited device (0.5 eV) whereas the bulk-limited device (0.2 eV) follows more closely the  $I \sim V^2$  behavior predicted by trap-free SCLC with constant mobilities. At high bias the curves converge.

$$b = \frac{J_{e,\text{cathode}} - J_{e,\text{anode}}}{J} = \frac{J_{h,\text{anode}} - J_{h,\text{cathode}}}{J} = \frac{\int_0^L eR(x)dx}{J}, \quad (10)$$

where  $L$  is the device thickness,  $R$  the recombination rate density [ $rpm$  in Eq. (3)], and  $J$  the averaged total current.

In an attempt to illustrate the beneficial use of small electron injection barriers, let us consider the current balance versus bias curve for TPD/Alq<sub>3</sub> bilayer devices with two different barrier heights, 0.2 and 0.5 eV; see Fig. 10. The device with the small electron injection barrier is bulk limited and shows ideal current balance over virtually the entire bias range considered. Even at low bias the electron injection barrier of 0.2 eV is a good enough contact to provide high electron density next to the cathode, which prevents holes from leaving the device without recombining. For comparison, a contact-limited case with 0.5 eV as the electron injecting barrier is calculated. In this case, current balance is low at low bias upon turnon and reaches unity only at high bias. Such a change in efficiency versus voltage was found experimentally when removing the beneficial LiF cathode layer.<sup>59,60</sup> Indications for a significant injection barrier even for a nominal barrier as low as 0.2 eV in the case of calcium was concluded from the absence of a TSCLC peak.<sup>55</sup> In support of this, Campbell and Smith<sup>72</sup> found injection barriers into Alq<sub>3</sub> from low-work-function metals such as magnesium, calcium, and samarium to exceed the nominal value and to be pinned at 0.6 eV. In order to illustrate the influence of the cathode barriers on the current–voltage characteristics, the inset shows a variation in the apparent power law behavior for the same two devices, each having identical mobility parameters. The slope in this log–log plot for the contact-limited case (0.5 eV) is higher (with a power above 3) whereas in the bulk-limited case (0.2 eV) the current follows more closely the  $I \sim V^2$  power law predicted for trap-free

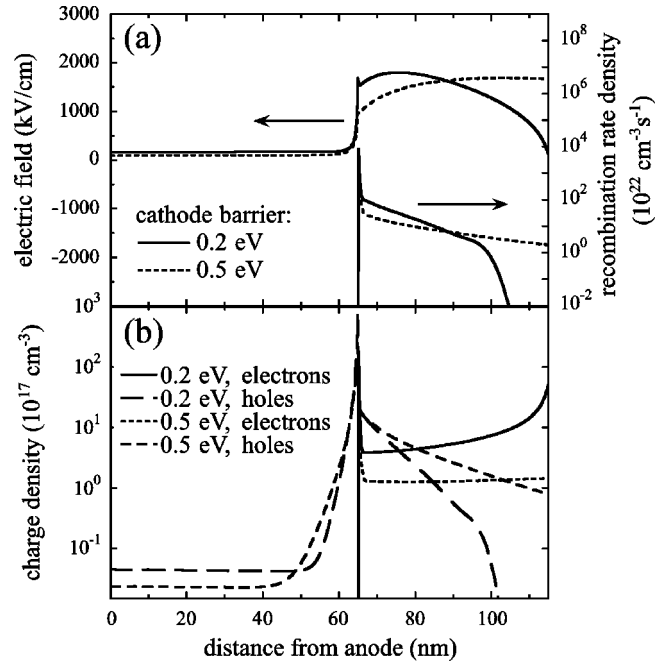


FIG. 11. (a) Electric field and recombination rate density as well as (b) charge densities for the two bilayer devices discussed in Fig. 10 at an applied voltage of 10 V with different electron injection barrier heights (0.2 and 0.5 eV). In the bulk-limited case (0.2 eV), the electric field is small at the cathode and reaches its maximum at the internal interface, where the charges accumulate on either side. In the contact-limited case (0.5 eV), holes may penetrate into Alq<sub>3</sub> and the electric field across the internal interface remains small. In this case, at high bias the number of exciting holes at the cathode decreases and current balance approaches unity.

SCLC with constant mobilities. At high bias the two curves converge.

Figure 11 illustrates the charge, electric field, and recombination rate density profiles at 10 V for the two cases of injection barriers. We note that in the case of the small cathode injection barrier, both the electron space-charge density near the cathode and the one at the internal interface are significantly higher. Therefore, the electric field is higher at the internal interface and smaller at the electrode than for the case of a high injection barrier. In fact, the electric field exhibits a local spike at the internal interface (due to the opposing hole accumulation layer) only for the small injection barrier case.

## V. TRILAYER DESIGNS

### A. Device structures

Here we consider three artificial OLEDs in order to compare the performance of different device design concepts. We use field-independent mobilities, a constant total layer thickness, and the same anode (5.0 eV) and cathode (3.3 eV) work functions for all devices to facilitate interpretation of the results. Figure 12 illustrates the energy level diagrams and layer thicknesses for the three structures considered, for which the parameters are listed in Table II. The hole mobility of the HTL is taken to be one order of magnitude higher than the electron mobility in the HTL. While the mobilities are taken to vary significantly in different layers, the injection barriers for the anode and cathode are chosen as symmetrical

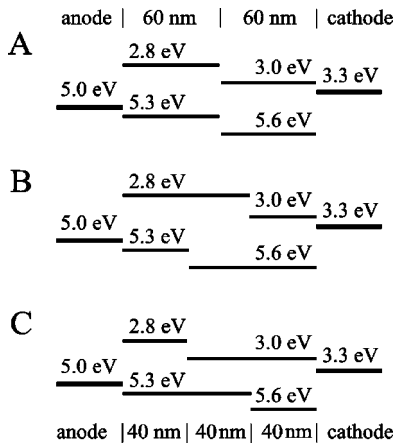


FIG. 12. Schematic energy level diagrams for bi- and trilayer devices. Symmetrical injection barriers of 0.3 eV for the both anode and cathode are chosen by taking the metal work functions as 5.0 and 3.3 eV, respectively.

(0.3 eV). The middle layer has the same hole mobility as the holes in the HTL and the same electron mobility as the electrons in the ETL. Therefore accumulation effects at interfaces are due to energy discontinuities only. Device A serves as a reference bilayer structure and is similar in nature to the TPD/Alq<sub>3</sub> device discussed in Secs. III and IV. Device B contains a high band gap material as the middle (emitting, or EML) layer, which causes the charges to accumulate on either interface and hence enhance the electric field across the middle layer. Device C represents an ideal structure in terms of both current balance and recombination since electrons and holes can enter the middle layer without overcoming an energy or mobility discontinuity and have a high chance to recombine in the same layer they are confined to by energy levels of the opposing transport layer. While the materials in the trilayer devices have the same transport properties, the HOMO/LUMO difference and therefore the emission color vary.

## B. Results

While all three structures have an optimal current balance of one in the entire voltage range considered, there are differences in the current and light output achieved. Because of its blocking nature, device B exhibits the smallest current and light output, while device C demonstrates the best performance. The bilayer structure is the intermediate case. Fig-

TABLE II. Mobility and energy level parameters for the artificial materials of the trilayer devices discussed in Sec. V.

Device structure	Layer	$\mu_e$ (cm <sup>2</sup> /V s)	$\mu_h$ (cm <sup>2</sup> /V s)	HOMO (eV)	LUMO (eV)
A	HTL	10 <sup>-7</sup>	10 <sup>-5</sup>	5.3	2.8
	ETL	10 <sup>-6</sup>	10 <sup>-7</sup>	5.6	3.0
B	HTL	10 <sup>-7</sup>	10 <sup>-5</sup>	5.3	2.8
	EML1	10 <sup>-6</sup>	10 <sup>-5</sup>	5.6	2.8
C	ETL	10 <sup>-6</sup>	10 <sup>-7</sup>	5.6	3.0
	HTL	10 <sup>-7</sup>	10 <sup>-5</sup>	5.3	2.8
	EML2	10 <sup>-6</sup>	10 <sup>-5</sup>	5.3	3.0
	ETL	10 <sup>-6</sup>	10 <sup>-7</sup>	5.6	3.0

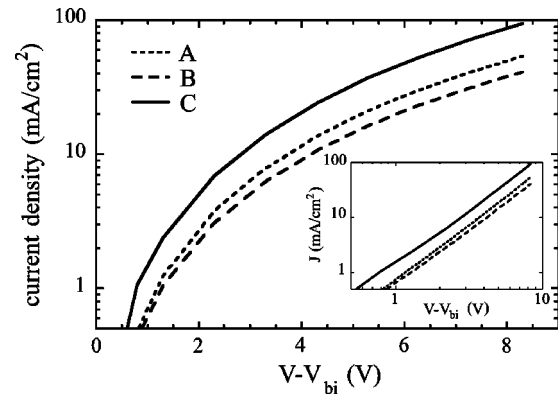


FIG. 13. Current–voltage characteristics of bi- and trilayer devices after correction of the built-in potential (1.7 eV). The inset, showing the current–voltage curve on a log–log scale, attests to the SCLC behavior ( $J \sim V^2$ ) for all three devices. Given that all devices have ideal current balance, device A will demonstrate the best power efficiency.

ure 13 shows the current–voltage characteristics for the three device structures. The inset, a log–log plot of the current–voltage curve, clearly demonstrates SCLC behavior ( $J \sim V^2$ ) for all three devices. Given that all three device structures exhibit ideal current balance, the current is a direct measure of the light output. The currents at an external bias of 10 V are 54, 41, and 95 mA/cm<sup>2</sup> for devices A, B, and C, respectively. Device C will therefore have the best power efficiency. For the sake of completeness, it must be added that a device with a single 120-nm-thick layer of the ETL material and the same electrodes shows poor performance, with current balance factors on the order of 10<sup>-4</sup> and a maximum current of 13 mA/cm<sup>2</sup> at 10 V. In support of these findings trilayer polymer LEDs were found to exhibit performance superior to single- or bilayer LEDs.<sup>12</sup>

Charge, recombination density, and electric field distributions are given in Figs. 14(a)–14(c) for the three devices considered. The recombination maximum is located in different layers, depending on the device structure. Bilayer device A has the maximum recombination in the ETL (at 60 nm). Device B’s maximum recombination is in the ETL (at 80 nm), with some penetration into the middle layer and a satellite at the HTL/EML interface (at 40 nm). Device C’s recombination zone is confined to the middle layer, with a maximum at the EML/ETL interface (at 80 nm) and a small satellite at the HTL/EML interface (at 40 nm). The electric field is plotted on a linear scale and has a local spike at the internal interface of bilayer device A [Fig. 14(a)]. The electric field in “charge-blocking” device B is highest in and uniform across the middle layer, into which little charge penetrates. In “charge-confining” device C, the electric field is highest across the ETL due to a strong pileup of the fast holes at the EML/ETL interface.

## VI. SUMMARY AND CONCLUSIONS

We have presented a numerical method to simulate multilayer OLEDs in both transient and steady-state operation using, as much as possible, experimentally determined material parameters. The results illustrate the operating prin-

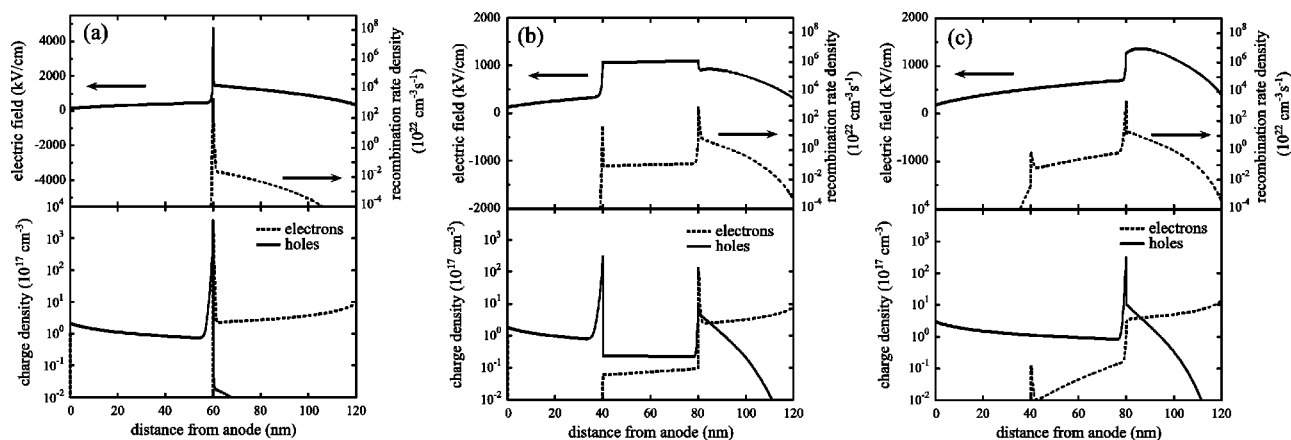


FIG. 14. Distribution of charge and recombination densities as well as electric field for devices A, B, and C. (a) Reference bilayer structure A, (b) trilayer structure B, and (c) trilayer structure C. In bilayer device A, the maximum recombination is located in the ETL at 60 nm. Device B has its highest recombination in the ETL at 80 nm with some penetration into the middle layer and a satellite at the HTL/EML interface (at 40 nm). Device C's recombination is primarily in the middle layer with a maximum to the left of the EML/ETL interface at 80 nm and a small satellite at the HTL/ETL interface (at 40 nm).

ciples of a commonly used  $\text{Alq}_3$  bilayer organic LED. In particular we arrived at the following conclusions.

(1) The algorithm reproduces the major features of the analytic solution for transient space-charge-limited currents in a monopolar single-layer device.

(2) The effect of injection barrier height on the transient current is demonstrated in a monopolar single-layer device. The suppressed current overshoot and a lower initial current for high injection barriers are indicative of contact-limited as opposed to space-charge-limited operation.

(3) The delayed onset of electroluminescence in a TPD/ $\text{Alq}_3$  bilayer device is determined by electrons crossing the ETL driven by an applied bias that is predominantly dropped across this layer. This is consistent with a previously determined field-dependent electron mobility in  $\text{Alq}_3$ .<sup>14</sup>

(4) The charges meet and give rise to initial electroluminescence within the bulk of the ETL, which subsequently shifts to the ETL/HTL interface. The transient electroluminescence exhibits a fast rise due to electron pileup at the ETL/HTL interface followed by a slow rise due to slow penetration of the holes into the ETL. Transient current and electroluminescence are comparable to experimental data.

(5) The recombination rate profile in this bilayer device is essentially a Dirac-delta function (less than 2 nm wide) at the interface, especially at high bias. This leads to an exciton density and therefore emission zone profile with a width given by the exciton diffusion length.

(6) Persistent electroluminescence due to residual charges follows the voltage turnoff with the possibility of a short-lived rise in electroluminescence. The strong residual space-charge field in this bilayer device may exceed the built-in field in magnitude, giving rise to a locally reversed field. A fast time scale determined by the removal of holes through the HTL and a slow time scale given by the migration of electrons in the ETL, with corresponding slowly decaying electroluminescence, can be distinguished.

(7) In  $\text{Alq}_3$  bilayer diodes the current balance versus bias curve is close to unity above turnon for small cathode injection barriers while for higher barriers it approaches unity

only at high bias, emphasizing the importance of cathode quality.

(8) Trilayer designs with ideal current balance were explored, and improved power efficiency due to charge confinement is demonstrated.

Further investigations will be directed at the influence of traps and dye dopants on the device characteristics and at finding suitable combinations of available materials in multilayer designs for further improvement of device performance.

## ACKNOWLEDGMENTS

The authors would like to thank George Malliaras for helpful discussions and the National Science Foundation for financial support (NSF GOALI Grant No. DMR 9704177). One of the authors (B.R.) is thankful to the Sunburst Fonds ETH.

- <sup>1</sup>C. W. Tang and S. A. VanSlyke, *Appl. Phys. Lett.* **51**, 913 (1987).
- <sup>2</sup>J. H. Burroughes, D. D. C. Bradley, A. R. Brown, R. N. Marks, K. Mackay, R. H. Friend, P. L. Burns, and A. B. Holmes, *Nature (London)* **347**, 539 (1990).
- <sup>3</sup>H. Bässler, Y. H. Tak, D. V. Khramtchenkov, and V. R. Nikitenko, *Synth. Met.* **91**, 173 (1997).
- <sup>4</sup>D. V. Khramtchenkov, H. Bässler, and V. I. Arkhipov, *J. Appl. Phys.* **79**, 9283 (1996).
- <sup>5</sup>J. C. Scott, S. Karg, and S. A. Carter, *J. Appl. Phys.* **82**, 1454 (1997).
- <sup>6</sup>G. G. Malliaras and J. C. Scott, *J. Appl. Phys.* **83**, 5399 (1998).
- <sup>7</sup>G. G. Malliaras and J. C. Scott, *J. Appl. Phys.* **85**, 7426 (1999).
- <sup>8</sup>P. S. Davids, I. H. Campbell, and D. L. Smith, *J. Appl. Phys.* **82**, 6319 (1997).
- <sup>9</sup>B. K. Crone, P. S. Davids, I. H. Campbell, and D. L. Smith, *J. Appl. Phys.* **87**, 1974 (2000).
- <sup>10</sup>J. Staudigel, M. Stössel, F. Steuber, and J. Simmerer, *J. Appl. Phys.* **86**, 3895 (1999).
- <sup>11</sup>V. Bliznyuk, B. Ruhstaller, P. J. Brock, U. Scherf, and S. A. Carter, *Adv. Mater.* **11**, 1257 (1999).
- <sup>12</sup>J. P. Chen, G. Klärner, J. I. Lee, D. Markiewicz, V. Y. Lee, R. D. Miller, and J. C. Scott, *Synth. Met.* **107**, 129 (1999).
- <sup>13</sup>D. J. Pinner, R. H. Friend, and N. Tessler, *J. Appl. Phys.* **86**, 5116 (1999).
- <sup>14</sup>S. Barth, P. Müller, H. Riel, P. F. Seidler, W. Riess, H. Vestweber, and H. Bässler, *J. Appl. Phys.* (in press).
- <sup>15</sup>D. J. Pinner, R. H. Friend, and N. Tessler, *Appl. Phys. Lett.* **76**, 1137 (2000).
- <sup>16</sup>V. Savvateev, A. Yakimov, and D. Davidov, *Adv. Mater.* **11**, 519 (1999).

- <sup>17</sup>V. R. Nikitenko, Y.-H. Tak, and H. Bässler, *J. Appl. Phys.* **84**, 2334 (1998).
- <sup>18</sup>N. Tessler, D. J. Pinner, V. Cleave, D. S. Thomas, G. Yahiolu, P. Le Barny, and R. H. Friend, *Appl. Phys. Lett.* **74**, 2764 (1999).
- <sup>19</sup>B. Ruhstaller, S. A. Carter, and J. C. Scott (unpublished).
- <sup>20</sup>P. W. M. Blom, M. J. M. de Jong, and S. Breedijk, *Appl. Phys. Lett.* **71**, 930 (1997).
- <sup>21</sup>It has previously been shown that the electrical response for voltages far from the flat band condition ( $|V - V_{\text{bi}}| \geq 0.5 \text{ V}$ ) is insensitive to the numerical value of  $D$  (Ref. 6).
- <sup>22</sup>U. Wolf, V. I. Arkhipov, and H. Bässler, *Phys. Rev. B* **59**, 7507 (1999).
- <sup>23</sup>J. C. Scott and G. G. Malliaras, *Chem. Phys. Lett.* **299**, 115 (1999).
- <sup>24</sup>L. Bozano, S. A. Carter, P. J. Brock, and J. C. Scott (unpublished).
- <sup>25</sup>Y. Shen, M. W. Klein, D. B. Jacobs, J. C. Scott, and G. G. Malliaras (unpublished).
- <sup>26</sup>J. C. Scott, G. G. Malliaras, J. R. Salem, P. J. Brock, L. Bozano, and S. A. Carter, *Proc. SPIE* **3476**, 111 (1998).
- <sup>27</sup>H. Ishii, K. Sugiyama, E. Ito, and K. Seki, *Adv. Mater.* **11**, 605 (1999).
- <sup>28</sup>E. Tutis, M.-N. Bussac, and L. Zuppiroli, *Appl. Phys. Lett.* **75**, 3880 (1999).
- <sup>29</sup>D. Emin, *Adv. Phys.* **18**, 305 (1975).
- <sup>30</sup>R. A. Marcus, *Annu. Rev. Phys. Chem.* **15**, 155 (1964).
- <sup>31</sup>V. G. Levich, *Adv. Electrochem. Electrochem. Eng.* **4**, 249 (1966).
- <sup>32</sup>A. Miller and E. Abrahams, *Phys. Rev.* **120**, 745 (1960).
- <sup>33</sup>J. Kalinowski, G. Giro, P. Di Marco, N. Camaioni, and V. Fattori, *Chem. Phys. Lett.* **265**, 607 (1997).
- <sup>34</sup>D. J. Fatemi, H. Murata, C. D. Merritt, and Z. H. Kafafi, *Synth. Met.* **85**, 1225 (1997).
- <sup>35</sup>J. J. M. Halls, K. Pichler, R. H. Friend, S. C. Moratti, and A. B. Holmes, *Appl. Phys. Lett.* **68**, 3120 (1996).
- <sup>36</sup>B. Ruhstaller, A. Breeze, A. Arango, and S. A. Carter (unpublished).
- <sup>37</sup>This is an approximation since there will be anomalous diffusion in amorphous systems.
- <sup>38</sup>H. Becker, A. Lux, A. B. Holmes, and R. H. Friend, *Synth. Met.* **85**, 1289 (1997).
- <sup>39</sup>M. Stössel *et al.*, *J. Appl. Phys.* **87**, 4467 (2000).
- <sup>40</sup>The mobility of holes in TPD is higher by approximately three orders of magnitude than the electron mobility in  $\text{Alq}_3$ .
- <sup>41</sup>While the average cell width is chosen as the hopping site separation, the cell width at interfaces are taken as three times smaller than in the middle of the layer.
- <sup>42</sup>P. M. Borsenberger and D. S. Weiss, *Organic Photoreceptors for Xerography* (Dekker, New York, 1998).
- <sup>43</sup>L. Bozano, S. A. Carter, J. C. Scott, G. G. Malliaras, and P. J. Brock, *Appl. Phys. Lett.* **74**, 1132 (1999).
- <sup>44</sup>J. C. Scott, S. Ramos, and G. G. Malliaras, *J. Imaging Sci. Technol.* **43**, 233 (1999).
- <sup>45</sup>A. G. Mückl, S. Berleb, W. Brütting, and M. Schwörer, *Synth. Met.* **111**, 91 (2000).
- <sup>46</sup>H. Vestweber, S. Barth, and W. Riess (private communication).
- <sup>47</sup>C. W. Tang, S. A. VanSlyke, and C. H. Chen, *J. Appl. Phys.* **65**, 3610 (1989).
- <sup>48</sup>R. G. Kepler, P. M. Beeson, S. J. Jacobs, R. A. Anderson, M. B. Sinclair, V. S. Valencia, and P. A. Cahill, *Appl. Phys. Lett.* **66**, 3618 (1995).
- <sup>49</sup>S. Naka, H. Okada, H. Onnagawa, Y. Yamaguchi, and T. Tsutsui, *Synth. Met.* **111**, 331 (2000).
- <sup>50</sup>T. Tsutsui, H. Tokuhisa, and M. Era, *Proc. SPIE* **3281**, 230 (1998).
- <sup>51</sup>I. Sokolik, R. Priestley, A. D. Walsler, R. Dorsinville, and C. W. Tang, *Appl. Phys. Lett.* **69**, 4168 (1996).
- <sup>52</sup>A. Many and G. Rakavy, *Phys. Rev.* **126**, 1980 (1962).
- <sup>53</sup>W. Helfrich and P. Mark, *Z. Phys.* **166**, 370 (1964).
- <sup>54</sup>A. J. Campbell, D. D. C. Bradley, H. Antoniadis, M. Inbasekaran, W. W. Wu, and E. P. Woo, *Appl. Phys. Lett.* **76**, 1734 (2000).
- <sup>55</sup>M. Stössel, J. Staudigel, F. Steuber, J. Blässing, and J. Simmerer, *Appl. Phys. Lett.* **76**, 115 (2000).
- <sup>56</sup>The initial drop in current is an artifact due to zero initial charge density combined with diffusion. However, in a real experiment this regime will be dominated by the  $RC$  time constant of the measuring circuit.
- <sup>57</sup>L. S. Hung, C. W. Tang, and M. G. Mason, *Appl. Phys. Lett.* **70**, 152 (1997).
- <sup>58</sup>G. E. Jabbour, Y. Kawabe, S. E. Shaheen, J. F. Wang, M. M. Morrell, B. Kippelen, and N. Peyghambarian, *Appl. Phys. Lett.* **71**, 1762 (1997).
- <sup>59</sup>W. Riess, H. Riel, P. F. Seidler, and H. Vestweber, *Synth. Met.* **99**, 213 (1999).
- <sup>60</sup>M. Stössel *et al.*, *Synth. Met.* **111**, 19 (2000).
- <sup>61</sup>D. M. Goldie, *J. Phys. D* **32**, 3058 (1999).
- <sup>62</sup>R. Treusch, F. J. Himpfel, S. Kakar, L. J. Terminello, C. Heske, T. van Buuren, V. V. Dinh, H. W. Lee, K. Pakbaz, G. Fox, and I. Jimenez, *J. Appl. Phys.* **86**, 88 (1999).
- <sup>63</sup>M. Hiramoto, K. Koyama, K. Nakayama, and M. Yokoyama, *Appl. Phys. Lett.* **76**, 1336 (2000).
- <sup>64</sup>F. Rohlfing, T. Yamada, and T. Tsutsui, *J. Appl. Phys.* **86**, 4978 (1999).
- <sup>65</sup>I. H. Campbell, M. D. Joswick, and I. D. Parker, *Appl. Phys. Lett.* **67**, 317 (1995).
- <sup>66</sup>M. Matsumura, A. Ito, and Y. Miyamae, *Appl. Phys. Lett.* **75**, 1042 (1999).
- <sup>67</sup>J. Lam, T. C. Gorjanc, Y. Tao, and M. D'Iorio, *J. Vac. Sci. Technol. A* **18**, 593 (2000).
- <sup>68</sup>K. Yamashita, J. Futenma, T. Mori, and T. Mizutani, *Synth. Met.* **111**, 87 (2000).
- <sup>69</sup>M. Matsumura and Y. Jinde, *Synth. Met.* **91**, 197 (1997).
- <sup>70</sup>V. R. Nikitenko, V. I. Arkhipov, Y.-H. Tak, J. Pommerehne, H. Bässler, and H.-H. Hörhold, *J. Appl. Phys.* **81**, 7514 (1997).
- <sup>71</sup>V. Savvateev, J. H. Friedl, L. Zou, J. Shinar, K. Christensen, W. Oldham, L. J. Rothberg, Z. Chen-Esterlit, and R. Kopelman, *Appl. Phys. Lett.* **76**, 1501 (2000).
- <sup>72</sup>I. H. Campbell and D. L. Smith, *Appl. Phys. Lett.* **74**, 561 (1999).